

# NIR Laser Responsive Nanoparticles for Ovarian Cancer Targeted Combination Therapy with Dual-modal Imaging Guidance

**Jiawen Zhao**

The First Affiliated Hospital of Chongqing Medical University <https://orcid.org/0000-0003-0289-6333>

**Liang Zhang**

The First Affiliated Hospital of Chongqing Medical University

**Yingjie Qi**

Dianjiang People's Hospital of Chongqing

**Kui Liao**

The First Affiliated Hospital of Chongqing Medical University

**Zhigang Wang**

Institute of Ultrasound Imaging, the Second Affiliated Hospital of Chongqing Medical University

**Ming Wen**

The First Affiliated Hospital of Chongqing Medical University

**Di Zhou** (✉ [zhoudi@cqmu.edu.cn](mailto:zhoudi@cqmu.edu.cn))

The First Affiliated Hospital of Chongqing Medical University <https://orcid.org/0000-0003-4205-8983>

---

## Research

**Keywords:** Bismuth sulfide, folic acid, chemotherapy, photothermal therapy

**Posted Date:** December 23rd, 2020

**DOI:** <https://doi.org/10.21203/rs.3.rs-131959/v1>

**License:** © ⓘ This work is licensed under a Creative Commons Attribution 4.0 International License.

[Read Full License](#)

---

# Abstract

**Background:** Multifunctional nanoparticles with targeted therapeutic function and diagnostic-imaging are of great interest in the domain of precision therapy. The synergetic photothermal therapy (PTT)/chemotherapy with the guidance of CT/PA imaging is greatly expected to precisely kill cancer cells.

**Results:** The synthesized FBPD NPs not only own excellent CT/PA imaging contrast increase ability but also reveal superior tumor-killing efficiency. The prepared FBPD NPs revealed excellent dispersity, great stability, outstanding optical properties. The release efficiency of Dox in FBPD NPs after laser irradiation was achieved 86.7%. Meanwhile, Liquid-gas phase conversion of perfluoropentane (PFP) induced by PTT was discovered and verified, which significantly enhanced the drug release efficiency in the tumor region. Furthermore, a photosensitizer irradiated by PTT engenders heat toward tumor region. According to CCK-8 assay, the cell viability of FBPD NPs + laser group reached 8.9%. In addition, in the cytotoxicity assay in vivo, the tumors in the FBPD NPs + laser group were completely ablated. These results revealed whether in vitro or in vivo, assessments on tumor-bearing mice proved that the precise inhibiting efficiency of PTT combined with FBPD NPs, which played a significant role in the inhibition of tumor growth.

**Conclusion:** The FBPD NPs was successfully fabricated, realizing CT/PA imaging-guided combination therapy against ovarian cancer. The unique nanoparticles with multiple abilities paves a emerging way toward precise treatment.

## 1. Background

Cancer has become one of the diseases that pose a severe threat to human health, the development of a more effective treatment against cancer has been attracting enormous interest [1]. Although conventional cancer treatments, including chemotherapy, radiotherapy, etc., have proved to be efficient, they are often associated with certain unignorable weaknesses, such as immune system depletion, high cost, patient nonadherence, and poor curative efficiency [2, 3]. These clinical problems have accordingly heightened the need for more specific and effective treatment of tumor ablation. These rising therapeutic projects should meet the rigorous demands of precise killing effect with the normal cells/tissue intact, which is currently approved as the potential substitutive therapeutic design to conventional treatment [4].

Among all the traditional treatments, chemotherapy is the most commonly used method for the clinical treatment of tumors [3, 5]. As one of the most widespread anthracycline anti-cancer drugs, doxorubicin (Dox), as an ordinary Food and Drug Administration (FDA) approved anti-cancer drug, kills tumor cells through a series of nuclear events, including DNA damage, apoptosis, and eventually cell death [6, 7]. However, the clinical application of Dox remains a challenge due to its low aqueous solubility, inadequate accumulation, and nonspecific distribution [8]. In the meanwhile, the effectiveness of Dox is always inevitably accompanied by various side effects, such as cardiac toxicity, gastrointestinal, and bone marrow suppression [9]. In order to mitigate the aforementioned adverse effects, drugs are encapsulated

by nanoparticles owing to their incomparable advantages such as non-toxicity and enhanced biocompatibility [10, 11]. More importantly, nanoparticles have been proved to boost drug solubility significantly and minimize the systematic toxicity of traditional antitumor agents, strengthening the therapeutic index ultimately [12]. Poly lactic-co-glycolic acid (PLGA) is a widely used FDA-approved biodegradable materials for anti-cancer drug delivery [13]. The diameter of PLGA nanospheres was described to be small enough to enable passive tumor targeting through the increased permeation and retention (EPR) effect [14]. Thus in this study, a Dox-loaded PLGA nanoparticle (PLGA-Dox) is applied in ovarian cancer treatment. In order to enhance the efficiency of cancer treatment, folic acid (FA) was chosen as the target as it is imperative in DNA synthesis and replication, cell proliferation, survival, and growth [15]. Noticeably, the FA receptor could be overexpressed in various tumor cells but rarely distributed in normal cells. Also, FA has been recognized to have several advantages such as lower molecular weight, immunogenicity, relatively high stability, and ease of modification [10, 11, 16].

In recent years, Photothermal therapy (PTT) has been performed as an emerging cancer treatment. Heat generated from the assimilation of optical energy via light-assimilating agents accumulated in the tumor area of post-NIR irradiation to kill tumor cells/tissues [17, 18]. Compared with visible light and ultraviolet, NIR laser is a safe light because of the little hurt to healthy and deep penetration [19]. Despite the efficient tumor ablation of PTT, the application is limited by the possible tumor reoccurrence induced by deficient hyperthermia or asymmetrical heat delivery within tumor areas [20]. One probable approach to optimize their therapeutic effects is to combine PTT with other types of treatments. It was reported that PTT and chemo-drug synergistically enhance the antitumor effect to a great extent [21–25]. Due to the post-X-ray bombardment, the secondary electrons were distributed to enhance the EPR effect, and consequently, high-Z nanomaterials could optimize the passive tumor targeting. As the atomic number is positively related to the photoelectric interaction, Bi nanoparticles are better than other elements [26]. Therefore, we considered bismuth sulfide ( $\text{Bi}_2\text{S}_3$ ) as a PTT agent on account of its outstanding biocompatibility and imaging performance. Furthermore, perfluoropentane (PFP), as a phase change material, would trigger the liquid-gas phase conversion and result in the generation of bubbles post laser irradiation, which could accelerate the tumor cells uptake of Dox [27].

Overall, with the rapid evolution of diagnostic-image technique, molecular imaging has been recognized as a burgeoning methods for accurate diagnosis guaranteed with high sensitivity and resolution. The establishment of multipurpose probes with the integrated function of cancer-targeting, imaging, and therapeutics are fundamental for accurate oncology [28]. In contrast to other different imaging methods, X-ray computed tomography (CT) is a mainstream clinical diagnostic strategy with advantages such as high resolution, little depth limitation, and permitting for three-dimensional (3D) reconstruction [29]. Besides, various internal limitations of CT imaging, especially low soft-tissue contrast and limited approachability, are vital factors that hinder the use of CT for clinical diagnosis [30, 31]. The performance of precision diagnosis can be optimized by the integration of CT with other imaging strategies that can uncover their preponderances. Comparatively, photoacoustic (PA) imaging, a nonionizing imaging form, transforms photon energy into acoustic pressure waves to obtain pictures, offering comparatively deeper

tissue penetration because of the less scattering of acoustic waves than light [4, 32]. Therefore, the design and synthesis of a therapeutic agent have become a major area of interest to effectuate the dual-modal imaging-guided treatment and concurrently maximize the virtue, safety, and precision of cancer treatment.

Herein, we designed the FA-targeted multifunctional NPs loading with Dox,  $\text{Bi}_2\text{S}_3$  and PFP to achieve an appealing tumor-targeted and dual-modal imaging-guided ovarian cancer combination therapy. In this nano-system,  $\text{Bi}_2\text{S}_3$  was used as the imaging contrast agent and PTT agent, while Dox served as the chemotherapy drug for the treatment of ovarian cancer. PFP as a phase change material, was further encapsulated in PLGA. After intravenous administration of FA- $\text{Bi}_2\text{S}_3$ -PFP-Dox-PLGA NPs (described as FBPD NPs), these NPs availablely accumulated into the tumor area assisted by active FA targeting after been injected into the mouse. Subsequently, the investigations in vitro and in vivo proved that the FBPD NPs manifest an excellent synergistic effect of PTT and chemotherapy with the guidance of CT and PA imaging, which considerably inhibited the tumor growth in mouse ovarian cancer models (Fig. 1).

Schematic illustration of the multipurpose nanoplatform for availablely CT/PA imaging-guided combination therapy to tumor cells/tissue.

## 2. Materials And Methods

### Materials

Dox was purchased from Beijing Bailingwei Technology Co., Ltd. (Mw = 579.99, China).  $\text{Bi}_2\text{S}_3$  modified by oleic acid and PLGA-PEG-FA were obtained from Xi'an Ruixi Biological Technology Co., Ltd. (China). Perfluoropentane (PFP) was obtained from Strem Chemicals, Inc. (America). Cell Counting Kit-8 (CCK-8) was obtained from Dojindo (Japan). The 2-(4-Amidinophenyl)-6-indolecarbamidinedihydrochloride (DAPI) and Trypsin-EDTA solution (0.25% trypsin) were obtained from Beyotime Technology. Dichloromethane ( $\text{CHCl}_2$ ) and isopropyl alcohol were obtained from Chongqing Chuan Dong Chemical Co., Ltd. (China). Poly (vinyl alcohol) (PVA), 1,1'-dioctadecyl-3,3,3',3'- tetramethylindotricarbocyanine iodide (DiR) and Dialysis membrane (10,000–12,000 Da) were obtained from Sigma-Aldrich Chemical Co., Ltd. (MW: 25,000, America). McCoy's 5A was obtained from Procell Life Science&Technology Co., Ltd.

### Synthesis of FPBD NPs

PLGA-PEG-FA encapsulating  $\text{Bi}_2\text{S}_3$ , PFP, and Dox (designed as FPBD NPs) was manufactured by a double emulsion (water/oil/ water: W/O/W) method [33]. First, 10 mg of Dox dissolved in 200  $\mu\text{L}$  of double distilled water; Then 400  $\mu\text{L}$  of PFP was added to the above solution, following by a probe sonication under the ice bath (100 W, 1 min). 200  $\mu\text{L}$  of  $\text{Bi}_2\text{S}_3$  and 50 mg PLGA-PEG-FA were dissolved in 3 mL of  $\text{CHCl}_2$ , which was mixed with the mixture prepared before. Immediately, the compound was emulsified with an ultrasonic probe to form the initial emulsion (100 W, 3 min, ice bath). For the second emulsion, 8 mL of PVA (w/v = 4%) was joined into the initial emulsion and mixed by probe sonication for 2 min

(100 W, ice bath). Subsequently, the second emulsion was diluted in 10 mL of isopropyl alcohol solution (w/v = 2%), and the as-prepared emulsion was stirred at an ice bath for 3 hours to volatilize  $\text{CHCl}_2$  fully. Finally, the FPBD NPs were collected after the centrifugation (10,000 rpm, 5 min, 4 °C). As for the preparation of FPB NPs or PBD NPs, the difference lies in the removal of FA or Dox. All operations were carried out in dark.

### **The characterization of FBPD NPs**

Scanning electron microscopy (SEM, Hitachi S-3400N, Japan) and transmission electron microscopy (TEM, Hitachi H-7600, Japan) were used to characterize the morphology and structure of the FPBD NPs. The Zeta potential and average diameter were determined by Malvern Zetasizer Nano ZS instrument (Malvern Instruments, UK). A UV – vis spectrophotometer (UV-3600, Shimadzu, Japan) was used to assess the UV – vis absorption spectra. The concentration of Dox was determined by a standard curve method using a UV – vis spectrometer. The concentration of  $\text{Bi}_2\text{S}_3$  was confirmed by inductively coupled plasma mass spectrometry (ICP-MS).

The release of Dox in vitro under laser irradiation was assessed by dialysis [34]. FPBD NPs was transferred into dialysis bags (MWCO:10,000 Da) that were placed into 50 mL PBS, with stirring (150 rpm) at 37 °C. FBPD NPs was irradiated with laser (1.5 W, 10 min) or not before stirring. 1 mL of dialysate was aliquoted from the flask at different points (1, 2, 3, 4, 6, 12, 24, and 48 h), and 1 mL fresh PBS was added to the flask to remain constant volume. All samples were stored in -20 °C before measurement. The absorbance of Dox in the above solutions was measured by UV-Vis spectrophotometer.

### **Cell culture**

The human ovarian cancer SKOV-3 cells line was acquired from Procell Life Science & Technology Co., Ltd. The cells were cultivated in McCoy's 5A medium and maintained in an incubator with 5%  $\text{CO}_2$  at 37 °C. When the cells were observed under the microscope to reach the logarithmic growth phase, 0.25% trypsin-EDTA was employed to harvest the cells for follow-up experiments.

### **In vitro cytotoxicity assay of FBPD NPs**

The SKOV-3 cells were cultivate in 96-well culture plates at a density of  $1 \times 10^4$  cells/well in McCoy's 5A medium at 37 °C in the condition of 5%  $\text{CO}_2$ , although the cells adhere to the plates. Then, fresh culture medium containing NPs at the concentration of 2 mg/mL was used to substitute the above culture medium. Incubation of 6 h later, the viability of cells was evaluated by the CCK-8 assay. An EL × 800 Universal Microplate Reader (Bio-Tek Instrument Inc., America) was used to record at the optical density (OD) at 450 nm. Seven treatment groups were set up in this experiment: the control group (Control), the group subjected to laser only (Laser only), the group operated with FPB NPs and laser (FPB NPs + laser), the group operated with BPD NPs (BPD NPs), the group operated with BPD NPs and laser (BPD NPs + laser), the group operated with FBPD NPs (FBPD NPs), and the group operated with FBPD NPs and laser

(FBPD NPs + laser). These groups treated by laser at an intensity of 1.5 W/cm<sup>2</sup> for 5 min. Finally, the viability of the cells was assessed by a standard CCK-8 assay.

### **In vitro targeting ability of FBPD NPs**

The cellular uptake effect of FBPD NPs was assessed by confocal laser scanning microscopy (CLSM) and flow cytometry. SKOV-3 cells in logarithmic growth were seeded into CLSM-exclusive culture dishes at a density of  $1 \times 10^5$  cells/well. After 24 h of culture, FBPD NPs and BPD NPs were added separately and incubated 0.5, 1, 2, 3, and 4 h, respectively. After co-incubation with nanoemulsions, the cells were washed with PBS, and fixed in paraformaldehyde (4%) for 15 min. After fixing the cells, SKOV-3 cells were incubated with DAPI fluorescein (300  $\mu$ L) for 15 min. Ultimately, these fluorescence pictures were obtained through CLSM. Furthermore, the quantitative intracellular uptake of FBPD NPs and BPD NPs were analyzed with flow cytometry. In detail, the cells were digested with trypsin (0.25%) after incubation with FBPD NPs or BPD NPs then suspended in PBS immediately. Finally, the flow cytometry was used to assess the phagocytosis rate.

### **Animal model**

All animals (female nude mice with the weight of 16–20 g and age of 6–8 W) were obtained from Chongqing Tengxin Biotechnology Co., Ltd. All the operation were executed under direction ratified by the Institutional Animal Care and Use Committee of Chongqing Medical University. To constructed SKOV-3 tumor-bearing mice models, SKOV-3 cells were suspended into McCoy's 5A medium and then injected subcutaneously to the flank of nude mice.

### **In vivo targeting ability of FBPD NPs**

To study the distribution of FBPD NPs in vivo, six SKOV-3 tumor-bearing mice were divided into two groups: FBPD NPs group and BPD NPs group (n = 3). Firstly, all the mice were injected with FBPD NPs or BPD NPs (200  $\mu$ L, 5 mg/mL) intravenously, then the fluorescence pictures were collected at certain moments (0, 0.5, 1, 2, 3, 4, 6, and 24 h) after injected NPs by a fluorescence system (Fx7 Ir Spectra, Vilber Lourmat, France). The excitation and emission wavelengths of 748 nm and 780 nm.

### **In vitro and in vivo CT Imaging**

A clinical CT-imaging system was used to conduct CT-imaging. FBPD NPs dissolved in PBS at different concentrations (0, 1, 2, 3, 4 and 5 mg/mL) were placed in a 2 mL eppendorf tube for CT imaging in vitro. The imaging parameters were set as follows: 170 mA, 80 kV, and 0.625 mm. The CT-signal intensities of ROI were measured. In the experiment of CT-imaging in vivo, SKOV-3 tumor-bearing mice were i.v. injected with FBPD NPs or BPD NPs solution (200  $\mu$ L, 5 mg/mL). Then CT imaging was conducted at different time points (0, 0.5, 1, 2, 3, 4, 6, and 24 h). Average CT signal intensity (SI) of the tumor area of the same slice was measured.

### **In vitro and in vivo PA Imaging**

A Vevo LAZR Photoacoustic Imaging System (VisualSonics Inc., Toronto, Canada) was employed to obtain PA images. For in vitro PA imaging, different concentrations of FBPD NPs (0, 1, 2, 3, 4, and 5 mg/mL) were dissolved in PBS, which was used for PA signal inspection and to assess the linear relation of the PA signal as a function of FBPD NPs concentration. As for PA imaging in vivo, the images were surveyed using SKOV-3 tumor-bearing mice, which were configured into two groups (FBPD NPs and BPD NPs) (n = 3). After i.v. injecting 200  $\mu$ L (5 mg/mL) BPD NPs or FBPD NPs solution, the homologous PA images were recorded at different time points (0, 0.5, 1, 2, 3, 4, 6 and 24 h). Then the PA signal intensity of each sample was analyzed by Vevo LAZR software.

### **In vitro photothermal imaging and photo-induced phase change experiment**

In order to verify the PTT effect, the FBPD NPs at different concentrations (0, 1, 2, 3, 4, and 5 mg/mL) was exposed to an 808 nm laser (1.5 W/cm<sup>2</sup>, 5 min), and the infrared thermal images and temperature were reserved by an infrared thermal imaging camera (Fotric 226, China). To further show the photothermal stability of Bi<sub>2</sub>S<sub>3</sub>, the NPs were irradiated by NIR laser (1.5 W/cm<sup>2</sup>) for 5 min (laser on), then naturally cooled to room temperature (laser off) for five cycles to indicate the cyclical temperature change of FBPD NPs. The infrared thermal images were also recorded. Furthermore, in the experiment of FBPD NPs photo-induced phase changed, the FBPD NPs were placed on an inverted fluorescence microscope post laser irradiation, and the changes before and after the irradiation were recorded.

### **In vivo tumor growth inhibition of FBPD NPs**

To further evaluate the in vivo chemotherapy /photothermal efficacy of FBPD NPs, seven groups were established as the in vivo experiment (n = 5). When the tumor volume reached approximately 50–80 mm<sup>3</sup>, the SKOV-3 tumor-bearing mice were subjected to different treatments as follows: a. the group was i.v. injected with saline solution (200  $\mu$ L) (control group); b. the group was treated with laser only (1.5 W/cm<sup>2</sup>, 5 min) (Laser only); c. the group was i.v. injected with FBP NPs (200  $\mu$ L, 5 mg/mL) followed by 808 nm laser (1.5 W/cm<sup>2</sup>, 5 min) 3 h later (FBP NPs + laser); d. the group was i.v. injected with BPD NPs (200  $\mu$ L) at the concentration of 5 mg/mL (BPD NPs). e. the group was i.v. injected with BPD NPs (200  $\mu$ L, 5 mg/mL) followed by 808 nm laser (1.5 W/cm<sup>2</sup>, 5 min) 3 h later (BPD NPs + laser); f. the group was i.v. injected with FBPD NPs (200  $\mu$ L, 5 mg/mL) (FBPD NPs); g. the group was i.v. injected with FBPD NPs (200  $\mu$ L, 5 mg/mL) followed by 808 nm laser (1.5 W/cm<sup>2</sup>, 5 min) 3 h later (FBPD NPs + laser). After various treatments, the changes in tumor-volume and the weight of each mouse were recorded every two days. The relative tumor volumes  $V/V_0$  ( $V_0$ : the initial tumor volume before the treatment) was used to express the tumor-volume changes. Collected the tumor tissues and the main organs (heart, liver, spleen, lung, and kidney) of one mouse of each group after treatment, and then steeped in a 4% paraformaldehyde solution. Ultimately, the primary organs were stained with H&E, and the tumor were stained with H&E, TUNEL and PCNA for histopathological analysis.

### **Biosafety assay of FBPD NPs.**

Twenty-five Balb/c mice were i.v. injected with FBPD NPs (5 mg/mL, 200  $\mu$ L) and were divided into five groups (1, 3, 7, 14, and 28 days after the injection). Five Balb/c mice were injected with saline as the control group. Blood samples were used for the blood index including routine blood and biochemistry, and the major organs were used for H&E staining.

### Statistical Analysis

All statistical analyses were executed with SPSS 20.0 software. Data were offered as mean  $\pm$  standard deviation. The significance of the data is analyzed according to a Student's t-test: \* $P < 0.01$ .

## 3. Results And Discussion

### Design, Synthesis, and Characterization of FBPD NPs

The multipurpose FBPD NPs were synthesized following the strategy as shown in Fig. 2a. The double-emulsion approach to synthesize FBPD NPs has been reported by our group before has been skillfully operated [35]. A series of characterizations have been conducted on the as-synthesized NPs. The TEM images (Fig. 2c) showed that the FBPD NPs had a well-defined spherical shape, and the SEM image (Fig. 2b) revealed that homogeneous size distribution of FBPD NPs. The mean hydrodynamic diameter of the FBPD NPs was  $295.3 \pm 40.3$  nm (Fig. 2d). The size range indicated that it could readily transport in the blood vessel and accumulate into tumor tissue via the representative enhanced permeability and retention (EPR) effect [33]. In addition, the zeta potential of FBPD NPs was  $(-7.99 \pm 6.66)$  mV. The EE and DL of the FBPD NPs were calculated by UV spectrophotometry. UV-spectra of Dox dispersed in saline at different concentrations (20, 25, 30, 35, 40, and 50  $\mu$ g/mL) and the corresponding relationship between concentrations of Dox and absorbance (Fig. 2e, 2f). The EE was  $(87.48 \pm 0.19\%)$  for  $\text{Bi}_2\text{S}_3$  and  $(25.21 \pm 3.05\%)$  for DOX, respectively. The DL was  $(3.38 \pm 0.07\%)$  for  $\text{Bi}_2\text{S}_3$  and  $(4.07 \pm 0.49\%)$  for DOX, respectively. The result displayed that FBPD NPs could carry oil-solute and soluble drugs. While these FBPD NPs could act as photothermal conversion agents for therapeutic tumor ablation, due to its excellent imaging performance, these FBPD NPs could be potentially used as contrast agents for CT and PA simultaneously during the therapy, offering guidance for subsequent photothermal ablation and evaluating the potential of treatment results post entering the tumor site.

Different releasing behaviors were observed for Dox for FBPD NPs when in the presence and absence of laser irradiation (Fig. 2g). The percentage of DOX released almost reached 46.2% at 4 h after laser irradiation, while the percentage of Dox released reached 49.7% at 48 h in the control group. This is probably due to the addition of phase-changing PFP into the FBPD NPs. The laser irradiation triggered the liquid-gas phase conversion and subsequently induced a faster release of Dox.

Morphology and characterization. **(a)** Schematic diagram for the fabrication of FBPD NPs. **(b)** SEM and **(c)** TEM of FHMP NPs. **(d)** Size distribution of FBPD NPs. **(e)** UV-spectra of FBPD NPs dispersed in saline in different concentrations (20, 25, 30, 35, 40, 45, 50  $\mu$ g/mL) and **(f)** corresponding relationship between

concentration of FBPD NPs and absorbance. **(g)** In vitro release of DOX in FBPD NPs with or without laser irradiation.

### **In vitro cytotoxicity assay of FBPD NPs**

The cytotoxicity against SKOV-3 cells was assessed by the CCK-8 protocol. As shown in Fig. 3, FBPD NPs with laser irradiation demonstrated more effective cell growth suppression than that of FBPD NPs group without laser irradiation. In addition, while both in the presence of laser irradiation, the group of FBPD NPs resulted in low cell viability. Furthermore, when compared with FBPD NPs group and BPD NPs group, it was found that added FA resulted in more significant growth inhibition on SKOV-3 cells. The result showed that the chemotherapeutic approach, combined with photothermal techniques had an excellent tumor-suppression. After connected with FA, it could more effectively deliver antitumor drugs to the tumor region, which will greatly improve the anti-cancer effects.

Relative cell viability of SKOV-3 cells after different treatments (n = 3, \*p < 0.01).

### **In vitro targeting ability of FBPD NPs**

Confocal microscopy and flow cytometry were used to investigate the intracellular uptake of FBPD NPs. As shown in CLSM images, NPs contained Dox present red fluorescence, and DAPI-labeled SKOV-3 cells exhibit blue fluorescence (Fig. 4a). As expected, in the treatment group, numerous FBPD NPs with red fluorescence were internalized within the cells after 3 h of co-incubation. On the other hand, only a few BPD NPs assembled within the cells in the control group. Flow detection shows the same trend (Fig. 4b). The group treated with FBPD NPs was observed with much stronger fluorescence in the cells than the group treated with BPD NPs, especially at 3 h after incubation, which demonstrated that FA-labelled NPs had the strongest accumulation ability.

In vitro targeting ability. **(a)** Intracellular uptake of BPD NPs and FBPD NPs as observed by CLSM after various intervals of incubation. The scale bars are 100  $\mu$ m. **(b)** Flow cytometry analysis of intracellular uptake of BPD NPs and FBPD NPs.

### **In vivo targeting ability of FBPD NPs**

To further verify the targeting efficiency in vivo, the SKOV-3 tumor-bearing mice model was created, and fluorescence pictures were executed at certain time points after the intravenous administration with DiI-labeled FBPD NPs or BPD NPs. After injection of DiI-stained FBPD NPs, strong fluorescence signals were observed in the tumor area, while only weak signals were found in tumors in mice treated with BPD NPs (Fig. 5a). According to Fig. 5b, the fluorescence intensities with tumor regions reached a peak at 3 hours after FBPD NPs administration. Furthermore, in order to determine the distribution of NPs in the body, main organs and tumors were collected 24 hours post-injection for excised fluorescence imaging (Fig. 5c), and the relevant fluorescence intensities were quantified (Fig. 5d).

In vivo targeting ability. **(a)** In vivo fluorescence imaging and tumor targeting of a mouse at 0, 0.5, 1, 2, 3, 4, 6, and 24 h post-injection of SKOV-3 tumor-bearing mice. **(b)** Quantitative fluorescence intensity of tumor tissue at different times ( $n = 3$ ). **(c)** Bio-distribution of DiR-labeled BPD NPs or FBPD NPs in major organs excised from mice at 24 h post-injection. **(d)** Quantitative bio-distribution of BPD NPs or FBPD NPs in mice as determined by the average FL intensities of organs and tumors. (Values are means  $\pm$  sd.,  $n = 3$ .)

### **In Vitro and In Vivo CT Imaging**

Based on deep tissue penetration and 3D structure imaging advantages, CT imaging is one of the most helpful diagnostic methods [36]. The high atomic number of bismuth has strong X-ray absorption ability, which can significantly improve the contrast of CT imaging. Furthermore, Bi-nanoparticles has the advantages of low toxicity, small particle size, long blood circulation time, and surface modification [37]. Therefore, the experiment investigated the CT contrast imaging both in vitro and in vivo of FBPD NPs. When in vitro, it has been found that as the concentration of FBPD NPs increased, the CT signal value also increased and showed a good linear relationship (Fig. 6a). The CT imaging property in vivo was further evaluated on SKOV-3 tumor-bearing mice. As shown in Fig. 6c, after i.v. injection of FBPD NPs or BPD NPs, the group of FBPD NPs showed an distinct bright effect within the tumor area. The CT signal intensities of the tumor regions were measured with Pacs software, and it showed that the CT signal value peaked at 3 h (Fig. 6b). Furthermore, the pseudo-colored images were also recorded, it clearly indicated the increasement of CT imaging. This result demonstrated that FA has excellent targeting properties; therefore, could FBPD NPs could be delivered to the tumor region efficiently.

In Vitro and In Vivo CT Imaging. **(a)** In vitro CT contrast images and CT values of FBPD NPs at different concentrations. **(b)** Changes of CT-signal intensities within tumor regions at corresponding time points. **(c)** In vivo CT images of tumors on SKOV-3 tumor-bearing mice after i.v. injection of BPD NPs or FBPD NPs as recorded at different time points. The top row shows black and white images, and bottom row represents the pseudo-colored images.

### **In vitro and in vivo PA imaging**

To evaluate the capability of FBPD NPs as a PA probe, PA images were obtained using FBPD NPs as the contrast agent both in vivo and in vitro. Compared with other imaging methods, PA imaging has very high sensitivity [20].  $\text{Bi}_2\text{S}_3$  has been used as a PA contrast agent because of its strong absorbance in the NIR region [31]. While applied in vitro, PA imaging performance of FBPD NPs dispersed in PBS at different concentrations were recorded (Fig. 7a). Furthermore, the PA signal intensities increased linearly with the concentration of NPs increased from 1–5 mg/mL, suggesting that FBPD NPs could effectively achieve PA imaging. During the in vivo assessment, PA imaging of SKOV-3 tumor-bearing mice was conducted at different time points after i.v. injection of BPD NPs or FBPD NPs (Fig. 7b), and the relevant quantitative analyses of PA intensities were executed (Fig. 7c). Before i.v. injection, the tumor showed only a weak PA signal. The PA signal reached the maximum approximately 3 h after injection with FBPD NPs. The reason

could be the actively tumor-targeting induced by FA modification tumor cells at 3 h, and specifically bind to the folate-receptor on the tumor surface resulting in a high degree of accumulation of FBPD NPs in the tumor. In contrast to the FBPD NPs injection, few PA signal was discovered after BPD NPs injection. These results demonstrated that FBPD NPs could be served as a excellent contrast agent for PA imaging, which achieves diagnostic-imaging guidance and monitoring during tumor therapy.

In vitro and in vivo PA imaging. **(a)** In vitro PA contrast images and PA values of FBPD NPs at different concentrations. **(b)** PA images of tumor regions in SKOV-3 bearing-mice after i.v. injections of BPD NPs or FBPD NPs at varied time intervals (0, 0.5, 1, 2, 3, 4, 6, and 24 h). **(c)** PA signal at tumor regions in SKOV-3 tumor-bearing mice.

### **Photothermal and Photo-induced Phase Change performance of FBPD NPs**

To assess the photothermal performance of FBPD NPs, the temperature changes of FBPD NPs aqueous solution were recorded by an infrared thermal imaging camera after the NIR irradiation (808 nm). After laser irradiation at  $1.5 \text{ W/cm}^2$  for 5 min, FBPD NPs showed a rapid temperature increase at all concentrations. Comparatively, the PBS did not show any obvious temperature rise as the given conditions (Fig. 8a). During the laser on-off cycles, the maximum temperature of FBPD NPs did not drop significantly after the cycle, indicated that it has good thermal stability (Fig. 8b).

In the experiment of photo-induced phase change, before laser irradiation, FBPD NPs did not change significantly under the optical microscope (Fig. 8c); After exposed to laser irradiation, FBPD NPs undergone a liquid-gas phase change, and the volume of FBPD NPs increases significantly (Fig. 8d). This result indicated that the NPs could easily transform into gas while heating to physiological temperature due to the lower boiling point of PFP [17]. The PFP had eventuated a phase change after being heated, then resulted in increase in the size of the FBPD NPs, which was subsequently more helpful for the release of drugs and the thermal ablation effect in the tumor area.

Photothermal and Photo-induced Phase Change performance. **(a)** Plot of temperature change ( $\Delta T$ ) of PBS and FBPD NPs at different concentrations (0, 1, 2, 3, 4, and 5 mg/mL) as a function of irradiation duration using an 808 nm laser ( $1.50 \text{ W/cm}^2$ ). **(b)** Cycled heating profiles of FBPD NPs (concentration:  $100 \mu\text{L}$ , 5 mg/mL) irradiated by an 808 nm laser ( $1.50 \text{ W/cm}^2$ ) for five laser on/off cycles. **(c)** The imaging of FBPD NPs under the optical microscope before an 808 nm laser ( $1.50 \text{ W/cm}^2$ ). **(d)** The imaging of FBPD NPs under the optical microscope after an 808 nm laser ( $1.50 \text{ W/cm}^2$ ).

### **In vivo cytotoxicity assay of FBPD NPs.**

The combination of PTT and chemotherapy, an efficient therapy for tumors, causes lesser damage to surrounding normal tissues. According to cytotoxicity assay in vitro, seven groups (control, laser only, FBPD NPs + laser group, BPD NPs group, BPD NPs + laser group, FBPD NPs group, and FBPD NPs + laser group) were performed to evaluate the therapeutic efficacy of FBPD NPs. After conducting different treatments, the inhibitory effect on SKOV-3 tumor growth is shown in Fig. 9b. The volumes of tumor and the weights

of mice were measured every two days (Fig. 9c, 9d), meanwhile, photographs of these mice were taken every two days for fourteen days after the therapy (Fig. 9a). The result displayed the the tumor volume in the FBPD NPs + laser group was much smaller than those of the other groups. It showed that chemotherapy combined photothermal therapy with FA-modification could inhibit tumor growth significantly. Compared to FBP NPs + laser group and laser only group, it was found that the tumor growth in FBP NPs + laser group was significantly inhibited, which indicated that laser irradiation with FBP NPs also showed a suppression effect on the tumor growth. The result demonstrated that FA-loaded NPs could deliver Dox and  $\text{Bi}_2\text{S}_3$  to the tumor area and specifically kill the tumor. Furthermore, it had been reported that hyperthermia at  $41^\circ\text{C}$ - $45^\circ\text{C}$  would incur a synergistic effect together with traditional therapeutic approaches es such as chemotherapy in tumor treatment [38]. Our experimental results presented consistency with reported mechanisms.

In vivo cytotoxicity. **(a)** Photographs of SKOV-3 tumor-bearing mice of seven groups taken during 14 d period after various treatments. **(b)** Photographs of tumors dissected from mice of seven groups after various treatments. **(c)** Time-dependent tumor volume curves of seven groups after various treatments (n = 5). **(d)** Time-dependent body weights of seven groups after various treatments (n = 5).

Hematoxylin-eosin (H&E) staining, proliferating cell nuclear antigen (PCNA) staining, and TdT-mediated dUTP Nick-End Labeling (TUNEL) staining on tumor slices better affirmed the synergistic PTT/ chemotherapy effect (Fig. 10a). As shown in the H&E-staining tumor sections, there were much more deformed nucleus in PTT/ chemotherapy group than tumor sections in other groups, prompting serious necrosis of tumor cells. Furthermore, the apoptosis of cancer cells in the FBP NPs + laser group was more serious than that in laser only group. The result of TUNEL and PCNA staining followed the parallel tendency. Representative apoptosis cells were prompted by brown nucleus in the TUNEL staining. PCNA staining on tumor slices showed the in vivo proliferative abilities of seven groups where proliferative tumor cells were stained into brown. The TUNEL and PCNA staining indicated that synergistic PTT + chemotherapy possessed the highest efficacy than other groups. In addition, heart, liver, spleen, lung, and kidney of mice were conducted H&E staining after the treatments to survey the relevant pathological toxicity. Insignificant negative effect was discovered during the treatment course for all groups, indicating no obvious histological damage in the treatment group (Fig. 10b).

**(a)** H&E, TUNEL and PCNA staining on tumor sections from SKOV-3 tumor-bearing mice after various treatments. **(b)** H&E staining of the major organs (heart, liver, spleen, lung, and kidney) of SKOV-3 tumor-bearing mice after different treatments. The scale bars are 50  $\mu\text{m}$ .

### **Biosafety assay of FBPD NPs**

In order to explored the short/long-term potential toxicity of FBPD NPs, a blood biochemical assay and H&E staining of major organs were verified on Balb/c mice. The result of blood biochemical revealed that negligible changes after different treatments (Fig. 11A), indicating the satisfactory biocompatibility of

FBPD NPs. In addition, no obvious damage to major tissues was discovered, suggesting the the high therapeutic biosafety of FBPD NPs (Fig. 11B).

Biosafety of FBPD NPs. (a) Assay of blood index after i.v. injection of FBPD NPs (n = 5). (b) Images of H&E stained slices of major organs (scale bar = 50  $\mu$ m).

## Conclusions

In summary, we successfully constructed multifunctional theranostic FBPD NPs for highly efficient PTT/chemotherapy combination therapy with dual CT/PA imaging guidance/monitoring. The cells/tissues growth inhibition was comprehensively confirmed both in vitro and in vivo. The thermal energy generated by laser irradiation and the DOX released after the phase changed exerted a strengthened therapeutic effect on tumor cells/tissues. Dox could be rapidly released under an on-site laser irradiation, thus with reduced toxicity to non-tumor regions. In vivo experiments showed that FBPD NPs after laser irradiation could effectively inhibit the growth of tumors, and the NPs effectly accumulated in tumor region assisted by FA guidance. Furthermore, these NPs enhanced CT/PA imaging both in vitro and in vivo, offering he potential for tumor treatment guidance/monitoring. Our study provided great insights on using FBPD NPs as a multifunctional cancer theranostics nanoplatform.

## Abbreviations

PTT: photothermal therapy; PFP: perfluoro-n-pentane; Dox: doxorubicin; FDA: Food and Drug Administration; PLGA: poly lactic-co-glycolic acid; EPR: enhanced permeation and retention; FA: folic acid;  $\text{Bi}_2\text{S}_3$ : bismuth sulfide; CT: computed tomography; 3D: three-dimensional; PA: photoacoustic; FBPD NPs: FA- $\text{Bi}_2\text{S}_3$ -PFP-Dox-PLGA nanoparticles; FBP NPs: FA- $\text{Bi}_2\text{S}_3$ -PFP-PLGA nanoparticles; BPD NPs:  $\text{Bi}_2\text{S}_3$ -PFP-PLGA nanoparticles; CCK-8: Cell Counting Kit-8; DAPI: 2-(4-Amidinophenyl)-6-indolecarbamidinedihydrochloride; DiR: 1,1'-dioctadecyl-3,3',3'- tetramethylindotricarbocyanine iodide;  $\text{CHCl}_2$ : dichloromethane; PVA: poly (vinyl alcohol); SEM: scanning electron microscopy; TEM: transmission electron microscopy; ICP-MS: inductively coupled plasma mass spectrometry; EE: encapsulation efficiency; DL: drug loading; OD: optical density; CLSM: confocal laser scanning microscopy; H&E: Hematoxylin-eosin; TUNEL: TdT-mediated dUTP Nick-End Labeling; PCNA: proliferating cell nuclear antigen.

## Declarations

### Ethics approval and consent to participate

All animal experiments were performed under direction approved by the Institutional Animal Care and Use Committee of Chongqing Medical University.

### Consent for publication

No applicable.

## Availability of data and materials

All data generated or analysed during this study are included in this published article.

## Competing interests

The authors declare that they have no competing interests.

## Funding

This work was supported by the National Natural Science Foundation of China Youth Science Foundation Project (NO.81801717).

## Author details

ZJ, WM, and ZD: Department of Radiology, the First Affiliated Hospital of Chongqing Medical University, Chongqing 400010, China; ZL: Department of Ultrasound, the First Affiliated Hospital of Chongqing Medical University, Chongqing 400010, China; WZ: Institute of Ultrasound Imaging, the Second Affiliated Hospital of Chongqing Medical University, Chongqing 400010, China; LK: Department of Oncology, the First Affiliated Hospital of Chongqing Medical University, Chongqing 400010, China; QY: Dianjiang People's Hospital of Chongqing, Chongqing 408300, China.

## Authors' contributions

ZJ drafted the paper. ZJ, ZL, QY, LK, WM., WZ and ZD analyzed data and revised the paper. ZJ and ZL designed the experiments. All authors read and approved the final manuscript.

## Acknowledgements

Not applicable.

## References

1. Wang Y , Liu X , Deng G , Sun J , Yuan H , Li Q ,et al. Se@SiO<sub>2</sub>-FA-CuS nanocomposites for targeted delivery of DOX and nano selenium in synergistic combination of chemo-photothermal therapy. *Nanoscale*. 2018;10:2866-2875.
2. Zhou Y, Hu Y, Sun W, Zhou B, Zhu J, Peng C,et al. Polyaniline-loaded  $\gamma$ -polyglutamic acid nanogels as a platform for photoacoustic imaging-guided tumor photothermal therapy. *Nanoscale*. 2017;9:12746-12754.
3. Byrne JD, Jen YJ, Desimone JM. Use of iontophoresis for the treatment of cancer. *J Control Release*. 2018;284:144-151.

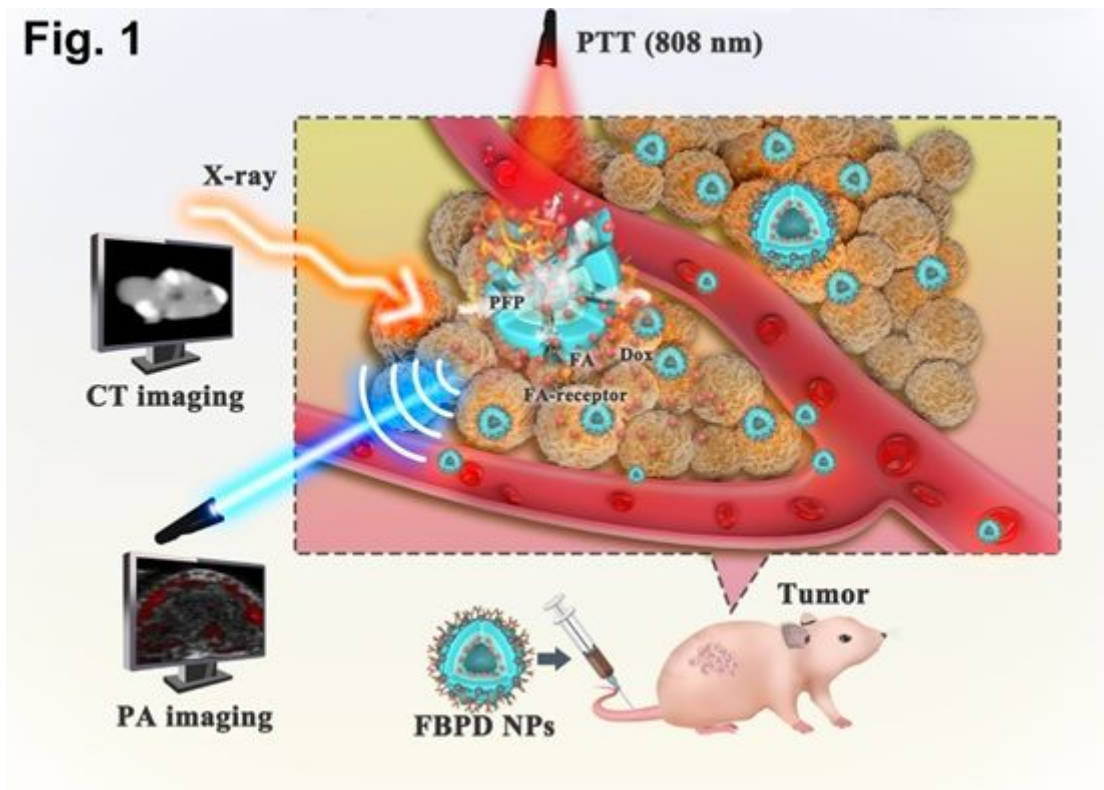
4. Huang J, Liu F, Han X, Zhang L, Hu Z, Jiang Q, et al. Nanosonosensitizers for Highly Efficient Sonodynamic Cancer Theranostics. *Theranostics*. 2018;8:6178-6194.
5. Liu P, Chen N, Yan L, Gao F, Ji D, Zhang S, et al. Preparation, characterisation and in vitro and in vivo evaluation of CD44-targeted chondroitin sulphate-conjugated doxorubicin PLGA nanoparticles. *Carbohydr Polym*. 2019;213:17-26.
6. Deshpande P, Jhaveri A, Pattni B, Biswas S, Torchilin V. Transferrin and octaarginine modified dual-functional liposomes with improved cancer cell targeting and enhanced intracellular delivery for the treatment of ovarian cancer. *Drug Delivery* 2018;25:517-532.
7. Shen X, Li T, Chen Z, Geng Y, Xie X, Li S, et al. Luminescent/magnetic PLGA-based hybrid nanocomposites: a smart nanocarrier system for targeted codelivery and dual-modality imaging in cancer theranostics. *Int J Nanomedicine*. 2017;12:4299-4322.
8. Mangal S, Gao W, Tonglei LI, Zhou QT. Pulmonary delivery of nanoparticle chemotherapy for the treatment of lung cancers: challenges and opportunities. *Acta Pharmacol Sin*. 2017;38:782-797.
9. Pan C, Liu Y, Zhou M, Wang W, Shi M, Xing M, et al. Theranostic pH-sensitive nanoparticles for highly efficient targeted delivery of doxorubicin for breast tumor treatment. *Int J Nanomedicine*. 2018;13:1119-1137.
10. Gao Z, Liu X, Deng G, Zhou F, Zhang L, Wang Q, et al. Fe<sub>3</sub>O<sub>4</sub>@mSiO<sub>2</sub>-FA-CuS-PEG nanocomposites for magnetic resonance imaging and targeted chemo-photothermal synergistic therapy of cancer cells. *Dalton Trans*. 2016;45:13456-13465.
11. Shen S, Li Y, Xiao Y, Zhao Z, Zhang C, Wang J, et al. Folate-conjugated nanobubbles selectively target and kill cancer cells via ultrasound-triggered intracellular explosion. *Biomaterials*. 2018;181:293-306.
12. Zhong Y, Su T, Shi Q, Feng Y, Tao Z, Huang Q, et al. Co-Administration Of iRGD Enhances Tumor-Targeted Delivery And Anti-Tumor Effects Of Paclitaxel-Loaded PLGA Nanoparticles For Colorectal Cancer Treatment. *Int J Nanomedicine*. 2019;14:8543-8560.
13. Li X, Jiang X. Microfluidics for producing poly (lactic-co-glycolic acid)-based pharmaceutical nanoparticles. *Adv Drug Deliv Rev*. 2018;128:101-114.
14. Cao Y, He J, Liu J, Zhang M, Ni P. Folate-Conjugated Polyphosphoester with Reversible Cross-Linkage and Reduction-Sensitivity for Drug Delivery. *ACS Appl Mater Interfaces*. 2018;10:7811-7820.
15. Tang Y, Li Y, Xu R, Li S, Hu H, Xiao C, et al. Self-assembly of folic acid dextran conjugates for cancer chemotherapy. *Nanoscale*. 2018;10:17265-17274.
16. Zang Y, Wei Y, Shi Y, Chen Q, Xing D. Chemo/Photoacoustic Dual Therapy with mRNA-Triggered DOX Release and Photoinduced Shockwave Based on a DNA-Gold Nanoplatform. *Small*. 2016;12:756-769.
17. Niu C, Xu Y, An S, Zhang M, Hu Y, Wang L, et al. loaded PLGA nanoparticles for photothermal tumor ablation. *Sci Rep*. 2017;7:5490.
18. Zhang N, Song J, Liu Y, Liu M, Zhang L, Sheng D, et al. Photothermal therapy mediated by phase-transformation nanoparticles facilitates delivery of anti-PD1 antibody and synergizes with antitumor immunotherapy for melanoma. *J Control Release*. 2019;306:15-28.

19. Lei P, An R, Zheng X, Zhang P, Du K, Zhang M, et al. Ultrafast synthesis of ultras-small polyethylenimine-protected AgBiS<sub>2</sub> nanodots by "rookie method" for in vivo dual-modal CT/PA imaging and simultaneous photothermal therapy. *Nanoscale*. 2018;10:16765-16774.
20. Zhang L, Wang D, Yang K, Sheng D, Tan B, Wang Z, et al. Mitochondria-Targeted Artificial "Nano-RBCs" for Amplified Synergistic Cancer Phototherapy by a Single NIR Irradiation. *Adv Sci (Weinh)*. 2018;5:1800049.
21. Li W, Peng J, Tan L, Wu J, Shi K, Qu Y, et al. Mild Photothermal Therapy/Photodynamic Therapy/Chemotherapy of Breast Cancer by Lyp-1 Modified Docetaxel/IR820 Co-loaded Micelles. *Biomaterials*. 2016;106:119-133.
22. Chen L, Zhou L, Wang C, Han Y, Lu Y, Liu J, et al. Tumor-Targeted Drug and CpG Delivery System for Phototherapy and Docetaxel-Enhanced Immunotherapy with Polarization toward M1-Type Macrophages on Triple Negative Breast Cancers. *Adv Mater*. 2019;31:e1904997.
23. Cheng L, He W, Gong H, Wang C, Chen Q, Cheng Z, et al. PEGylated Micelle Nanoparticles Encapsulating a Non-Fluorescent Near-Infrared Organic Dye as a Safe and Highly-Effective Photothermal Agent for In Vivo Cancer Therapy. *Adv.Funct.Mater*. 2013;23: 5893-5902.
24. Meng Z, Wei F, Wang R, Xia M, Chen Z, Wang H, et al. NIR-Laser-Switched In Vivo Smart Nanocapsules for Synergic Photothermal and Chemotherapy of Tumors. *Adv Mater*. 2016;28:245-253.
25. Zhang D, Cui P, Dai Z, Yang B, Yao X, Liu Q, et al. Tumor microenvironment responsive FePt/MoS<sub>2</sub> nanocomposites with chemotherapy and photothermal therapy for enhancing cancer immunotherapy. *Nanoscale*. 2019;11:19912-19922.
26. Chen Y, Zhao G, Wang S, He Y, Han S, Du C, et al. Platelet-membrane-camouflaged bismuth sulfide nanorods for synergistic radio-photothermal therapy against cancer. *Biomater Sci*. 2019;7:3450-3459.
27. Yang M, Zhang N, Zhang T, Yin X, Shen J. Fabrication of doxorubicin-gated mesoporous polydopamine nanoplat-forms for multimode imaging-guided synergistic chemophotothermal therapy of tumors. *Drug Deliv*. 2020;27:367-377.
28. Zhang HK, Chen Y, Kang J, Lisok A, Minn I, Pomper MG, et al. Prostate-specific membrane antigen-targeted photoacoustic imaging of prostate cancer in vivo. *Biophotonics*. 2018;11:e201800021.
29. Liu J, Zheng X, Yan L, Zhou L, Tian G, Yin W, et al. Bismuth Sulfide Nanorods as a Precision Nanomedicine for in Vivo Multimodal Imaging-Guided Photothermal Therapy of Tumor. *ACS Nano*. 2015;9:696-707.
30. Wang X, Ai A, Yu Z, Deng M, Liu W, Zhou G, et al. Dual-modal non-invasive imaging in vitro and in vivo monitoring degradation of PLGA scaffold based gold nanoclusters. *Mater Sci Eng C Mater Biol Appl*. 2020;107:110307.
31. Zhou D, Li C, He M, Ma M, Li P, Gong Y, et al. Folate-targeted perfluorohexane nanoparticles carrying bismuth sulfide for use in US/CT dual-mode imaging and synergistic high-intensity focused ultrasound ablation of cervical cancer. *J Mater Chem B*. 2016;4:4164-4181.

32. Chen S, Liu Y, Zhu S, Chen C, Xie W, Xiao L, et al. Dual-mode imaging and therapeutic effects of drug-loaded phase-transition nanoparticles combined with near-infrared laser and low-intensity ultrasound on ovarian cancer. *Drug Deliv.* 2018;25:1683-1693.
33. Xiong J, Feng J, Qiu L, Gao Z, Li P, Pang L, et al. SDF-1-loaded PLGA nanoparticles for the targeted photoacoustic imaging and photothermal therapy of metastatic lymph nodes in tongue squamous cell carcinoma. *Int J Pharm.* 2019;554:93-104.
34. Zhang L, Qin Y, Zhang Z, Fan F, Huang C, Lu L, et al. Dual pH/reduction-responsive hybrid polymeric micelles for targeted chemo-photothermal combination therapy. *Acta Biomater.* 2018;75:371-385.
35. Deng L, Cai X, Sheng D, Yang Y, Strohm EM, Wang Z, et al. A Laser-Activated Biocompatible Theranostic Nanoagent for Targeted Multimodal Imaging and Photothermal Therapy. *Theranostics.* 2017;7:4410-4423.
36. Liu Y, Li L, Guo Q, Wang L, Liu D, Wei Z, et al. Novel Cs-Based Upconversion Nanoparticles as Dual-Modal CT and UCL Imaging Agents for Chemo-Photothermal Synergistic Therapy. *Theranostics.* 2016;6:1491-1505.
37. Li Z, Hu Y, Chang M, Howard KA, Fan X, Sun Y, et al. Howard KA, Fan X, Sun Y, et al. Highly porous PEGylated Bi<sub>2</sub>S<sub>3</sub> nano-urchins as a versatile platform for in vivo triple-modal imaging, photothermal therapy and drug delivery. *Nanoscale.* 2016;8:16005-16016.
38. Mohammadi Gazestani A, Khoei S, Khoei S, Emamgholizadeh Minaei S, Motevalian M. In vivo evaluation of the combination effect of near-infrared laser and 5-fluorouracil-loaded PLGA-coated magnetite nanographene oxide. *Artif Cells Nanomed Biotechnol.* 2018;46:25-33.

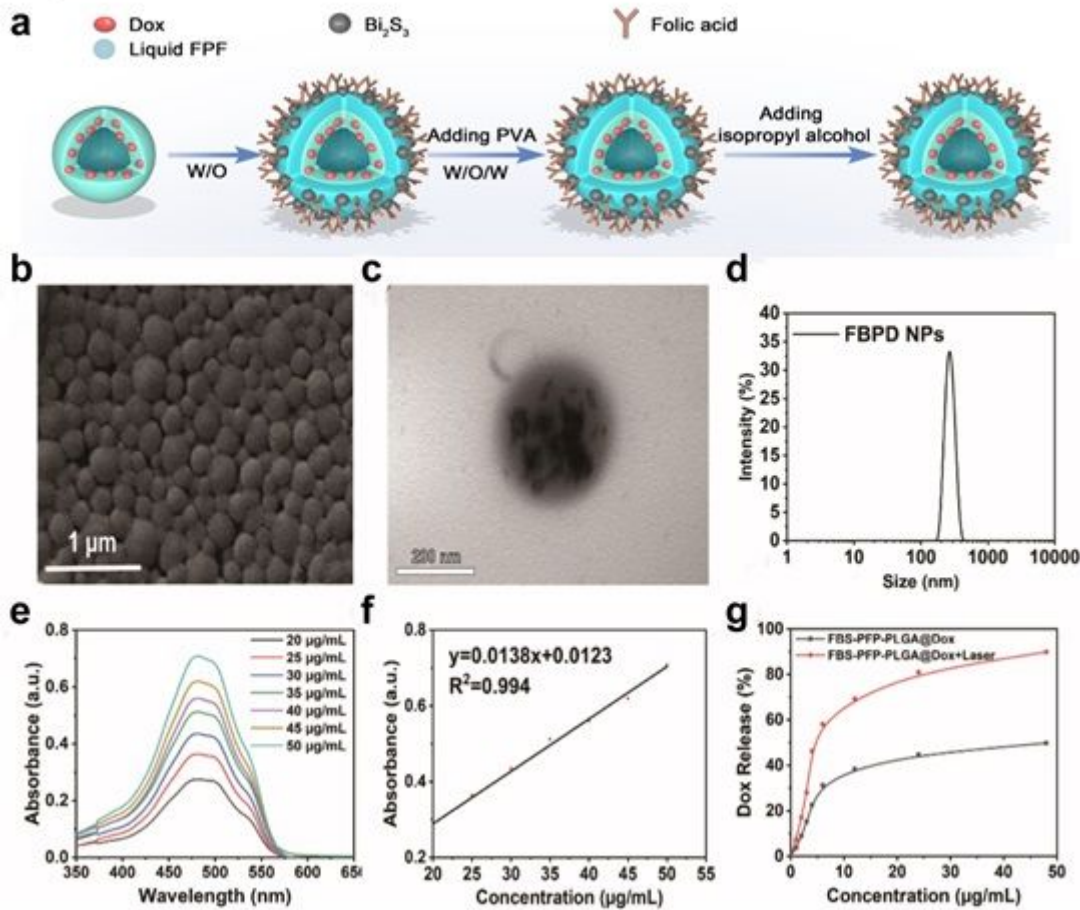
## Figures

**Fig. 1**



**Figure 1**

Schematic illustration of the multipurpose nanoplateform for available CT/PA imaging-guided combination therapy to tumor cells/tissue.

**Fig. 2****Figure 2**

Morphology and characterization. (a) Schematic diagram for the fabrication of FBPD NPs. (b) SEM and (c) TEM of FBPD NPs. (d) Size distribution of FBPD NPs. (e) UV-spectra of FBPD NPs dispersed in saline in different concentrations (20, 25, 30, 35, 40, 45, 50  $\mu\text{g/mL}$ ) and (f) corresponding relationship between concentration of FBPD NPs and absorbance. (g) In vitro release of DOX in FBPD NPs with or without laser irradiation.

Fig. 3

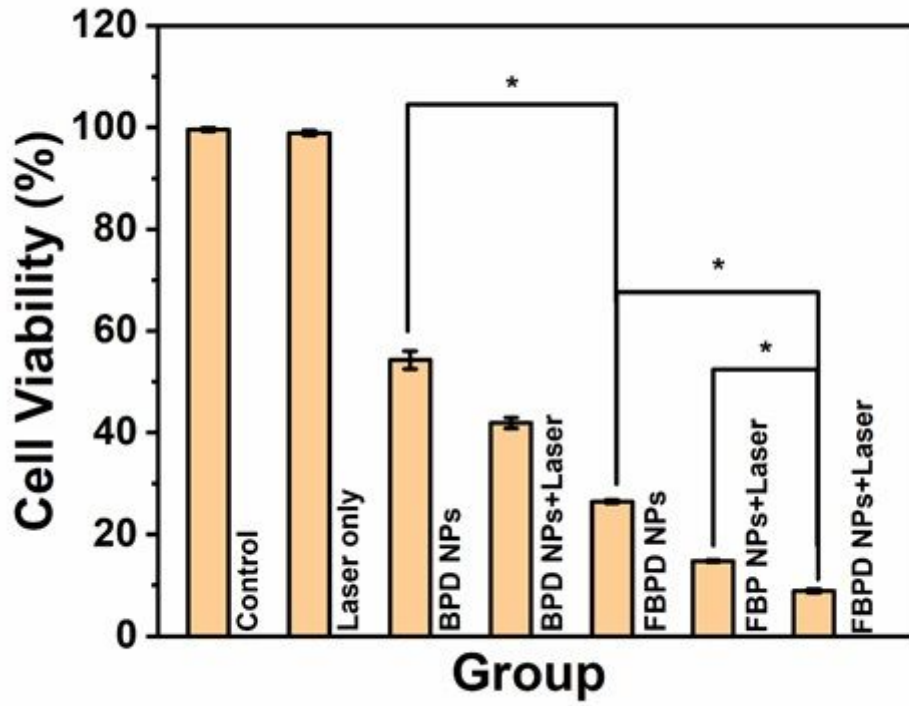
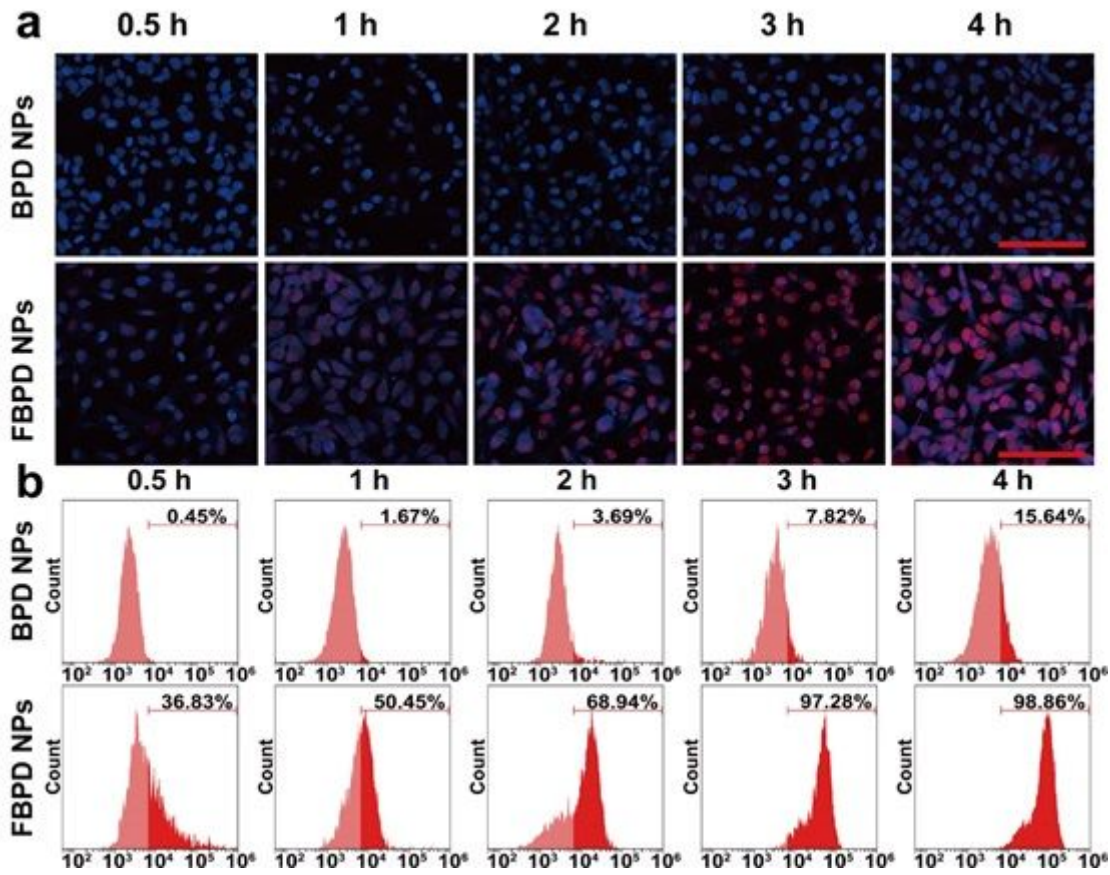


Figure 3

Relative cell viability of SKOV-3 cells after different treatments (n = 3, \*p < 0.01).

**Fig.4**



**Figure 4**

In vitro targeting ability. (a) Intracellular uptake of BPD NPs and FBPD NPs as observed by CLSM after various intervals of incubation. The scale bars are 100  $\mu$ m. (b) Flow cytometry analysis of intracellular uptake of BPD NPs and FBPD NPs.

**Fig. 5**

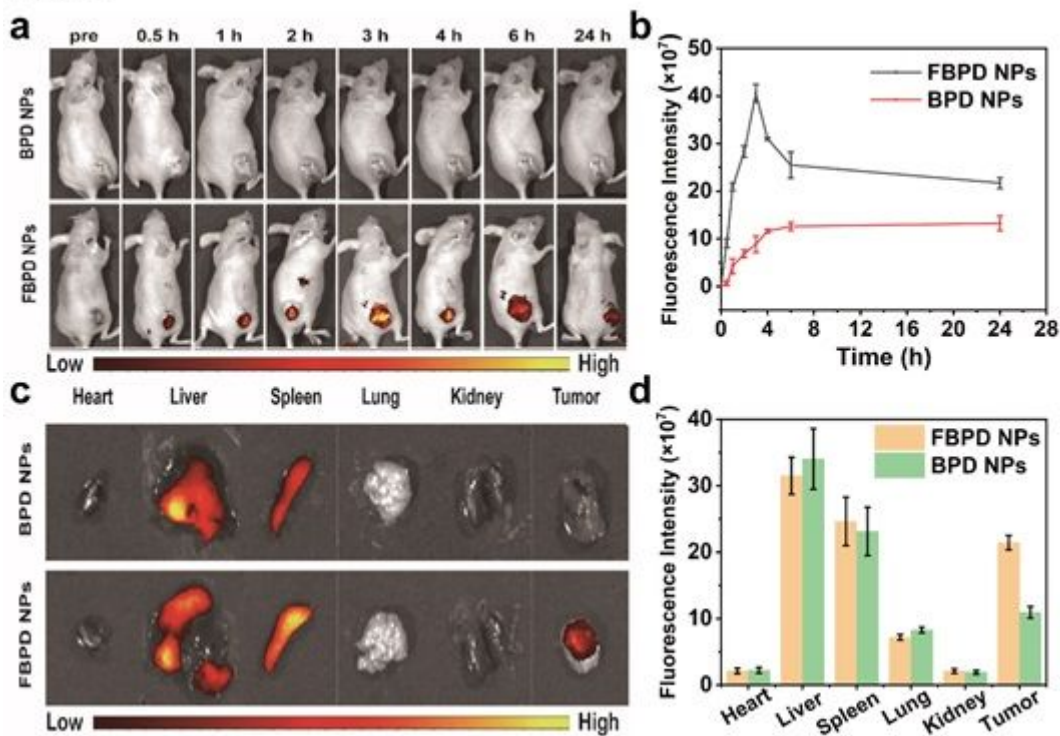


**Figure 5**

In vivo targeting ability. (a) In vivo fluorescence imaging and tumor targeting of a mouse at 0, 0.5, 1, 2, 3, 4, 6, and 24 h post-injection of SKOV-3 tumor-bearing mice. (b) Quantitative fluorescence intensity of tumor tissue at different times (n = 3). (c) Bio-distribution of DiR-labeled BPD NPs or FBPD NPs in major organs excised from mice at 24 h post-injection. (d) Quantitative bio-distribution of BPD NPs or FBPD NPs in mice as determined by the average FL intensities of organs and tumors. (Values are means  $\pm$  sd., n = 3.)

**Fig. 6**

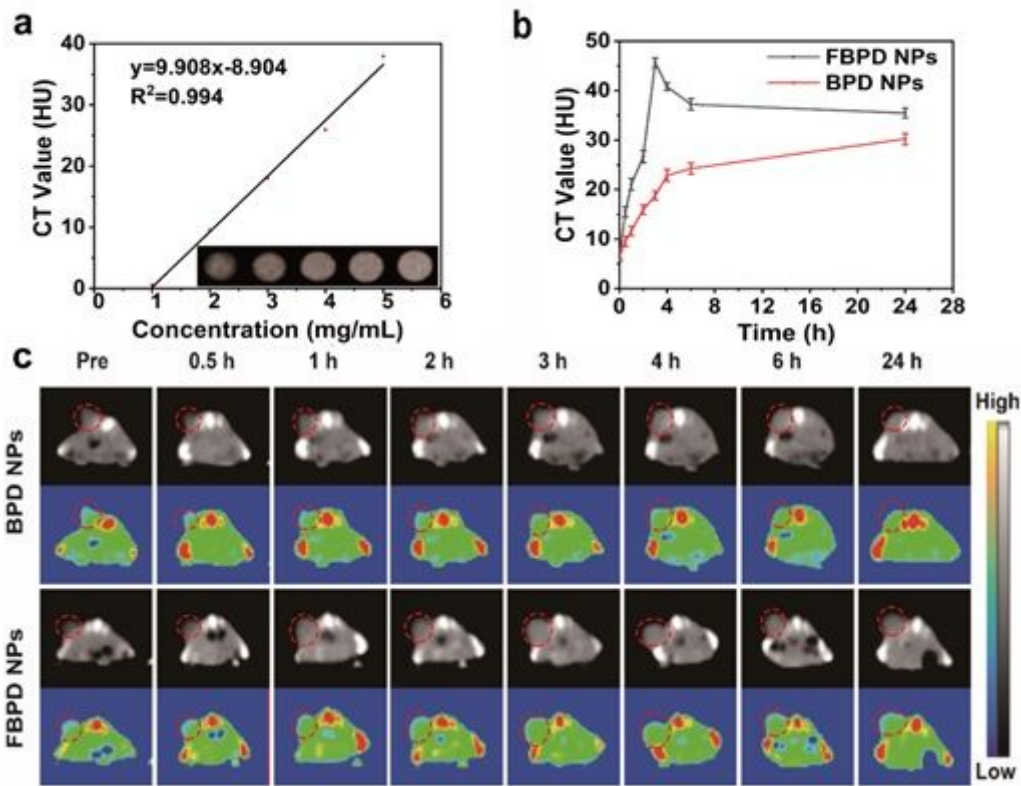


**Figure 6**

In Vitro and In Vivo CT Imaging. (a) In vitro CT contrast images and CT values of FBPD NPs at different concentrations. (b) Changes of CT-signal intensities within tumor regions at corresponding time points. (c) In vivo CT images of tumors on SKOV-3 tumor-bearing mice after i.v. injection of BPD NPs or FBPD NPs as recorded at different time points. The top row shows black and white images, and bottom row represents the pseudo-colored images.

**Fig. 7**

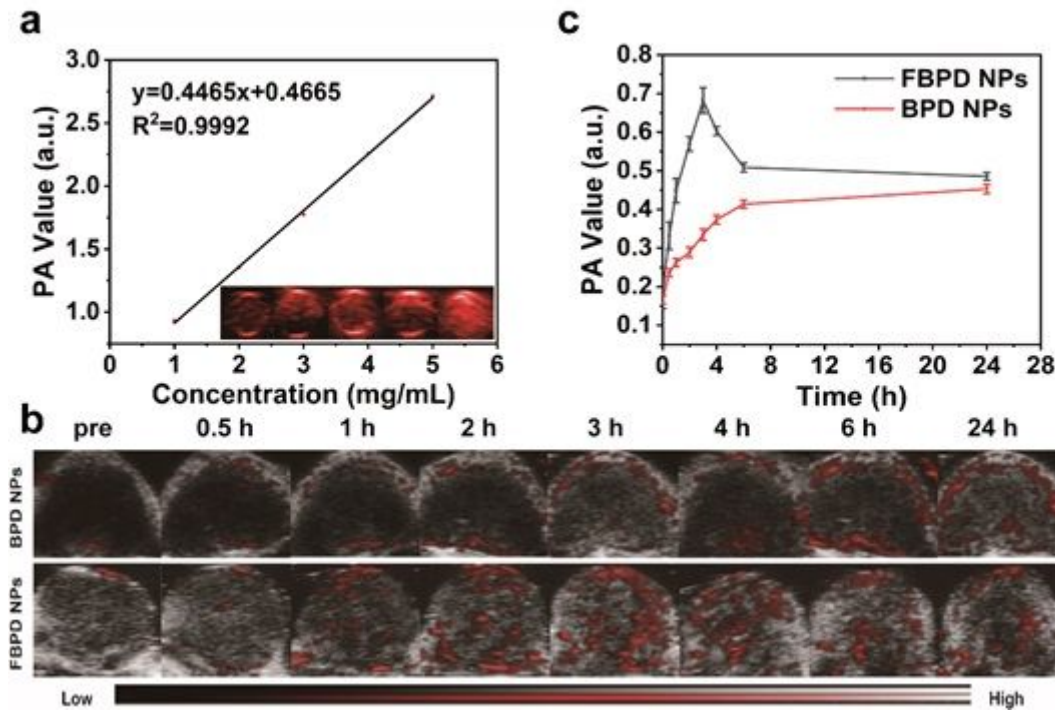


**Figure 7**

In vitro and in vivo PA imaging. (a) In vitro PA contrast images and PA values of FBPD NPs at different concentrations. (b) PA images of tumor regions in SKOV-3 bearing-mice after i.v. injections of BPD NPs or FBPD NPs at varied time intervals (0, 0.5, 1, 2, 3, 4, 6, and 24 h). (c) PA signal at tumor regions in SKOV-3 tumor-bearing mice.

**Fig. 8**

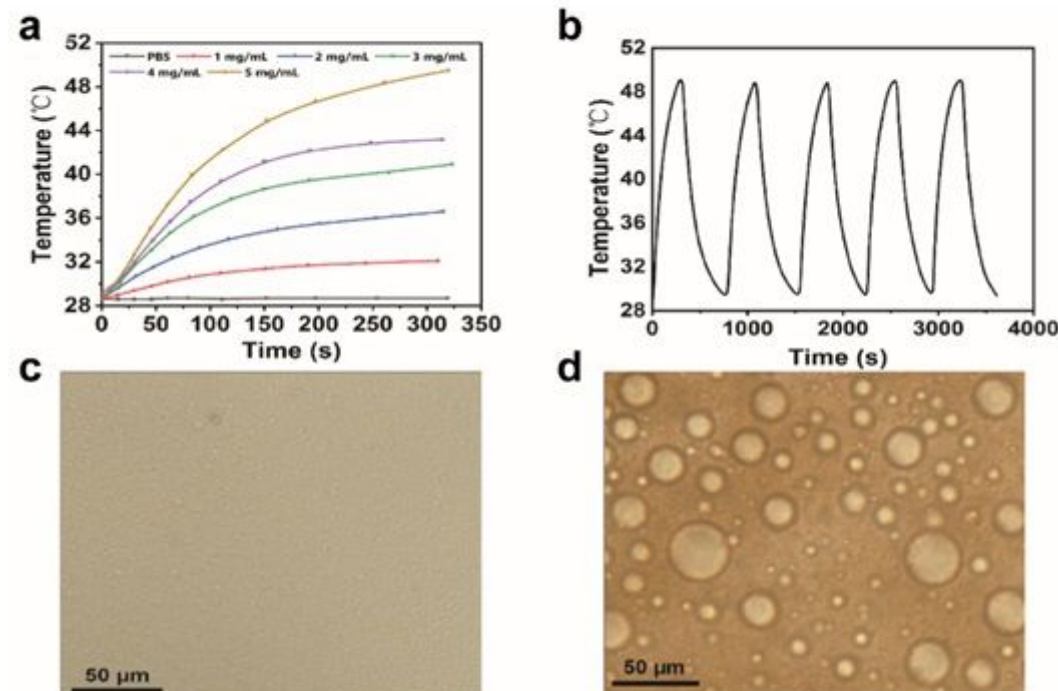


**Figure 8**

Photothermal and Photo-induced Phase Change performance. (a) Plot of temperature change ( $\Delta T$ ) of PBS and FBPD NPs at different concentrations (0, 1, 2, 3, 4, and 5 mg/mL) as a function of irradiation duration using an 808 nm laser (1.50 W/cm<sup>2</sup>). (b) Cycled heating profiles of FBPD NPs (concentration: 100  $\mu$ L, 5 mg/mL) irradiated by an 808 nm laser (1.50 W/cm<sup>2</sup>) for five laser on/off cycles. (c) The imaging of FBPD NPs under the optical microscope before an 808 nm laser (1.50 W/cm<sup>2</sup>). (d) The imaging of FBPD NPs under the optical microscope after an 808 nm laser (1.50 W/cm<sup>2</sup>).

**Fig. 9**

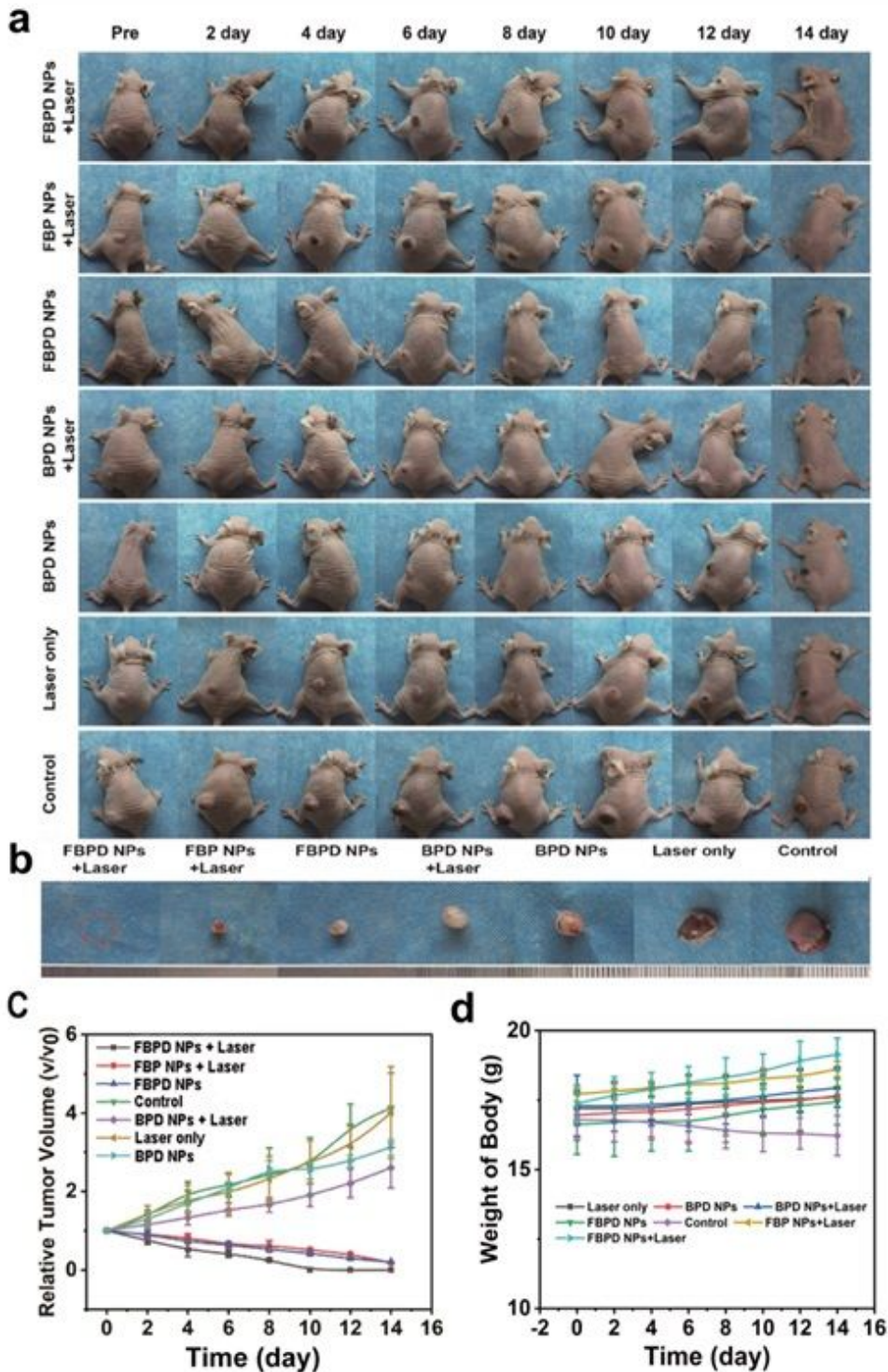
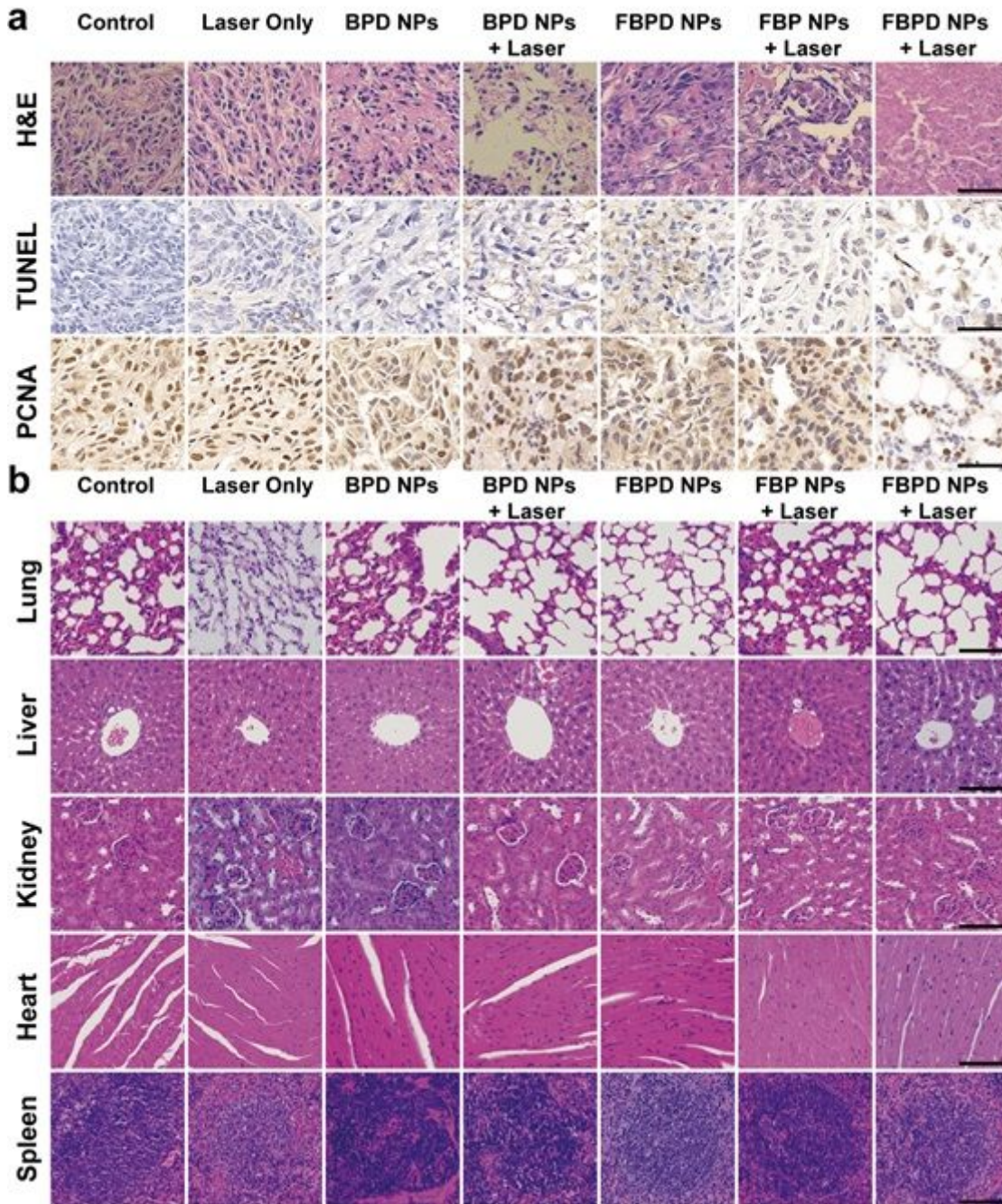


Figure 9

In vivo cytotoxicity. (a) Photographs of SKOV-3 tumor-bearing mice of seven groups taken during 14 d period after various treatments. (b) Photographs of tumors dissected from mice of seven groups after various treatments. (c) Time-dependent tumor volume curves of seven groups after various treatments (n = 5). (d) Time-dependent body weights of seven groups after various treatments (n = 5).

**Fig. 10**



**Figure 10**

(a) H&E, TUNEL and PCNA staining on tumor sections from SKOV-3 tumor-bearing mice after various treatments. (b) H&E staining of the major organs (heart, liver, spleen, lung, and kidney) of SKOV-3 tumor-bearing mice after different treatments. The scale bars are 50  $\mu$ m.

**Fig. 11**

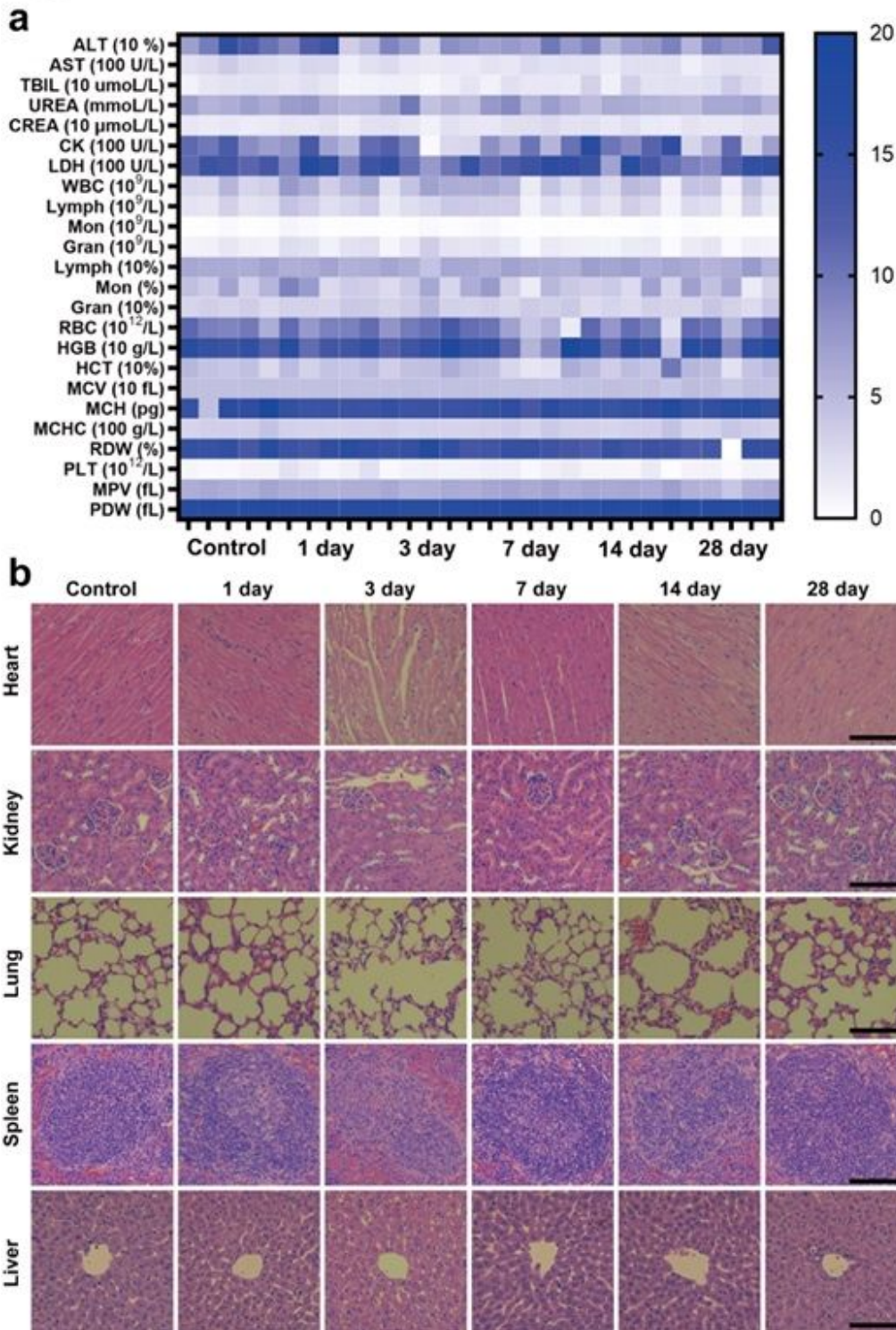


**Figure 11**

Biosafety of FBPD NPs. (a) Assay of blood index after i.v. injection of FBPD NPs (n = 5). (b) Images of H&E stained slices of major organs (scale bar = 50  $\mu$ m).